IOP Publishing | Institute of Physics and Engineering in Medicine Physics in Medicine & Biology

Phys. Med. Biol. **62** (2017) 7814–7832 https://doi.org/10.1088/1361-6560/aa8851

Subject-specific bone attenuation correction for brain PET/MR: can ZTE-MRI substitute CT scan accurately?

Maya Khalifé[1,2], Brice Fernandez[3], Olivier Jaubert[1], Michael Soussan[2], Vincent Brulon[2], Irène Buvat[2] and Claude Comtat[2]

[1] Institut du Cerveau et de la Moelle épinière (ICM), CNRS UMR 7225—Inserm U1127—Université Paris 6 UPMC UMR S1127, Paris, France
[2] Laboratoire Imagerie Moléculaire *In Vivo* (IMIV), UMR 1023 Inserm/CEA/Université Paris Sud—ERL 9218 CNRS, CEA/I2BM/SHFJ, Orsay, France
[3] Applications and Workflow, GE Healthcare, Orsay, France

E-mail: maya.khalife@icm-institute.org

Received 20 April 2017, revised 31 July 2017
Accepted for publication 24 August 2017
Published 20 September 2017

Abstract

In brain PET/MR applications, accurate attenuation maps are required for accurate PET image quantification. An implemented attenuation correction (AC) method for brain imaging is the single-atlas approach that estimates an AC map from an averaged CT template. As an alternative, we propose to use a zero echo time (ZTE) pulse sequence to segment bone, air and soft tissue. A linear relationship between histogram normalized ZTE intensity and measured CT density in Hounsfield units (HU) in bone has been established thanks to a CT-MR database of 16 patients. Continuous AC maps were computed based on the segmented ZTE by setting a fixed linear attenuation coefficient (LAC) to air and soft tissue and by using the linear relationship to generate continuous μ values for the bone. Additionally, for the purpose of comparison, four other AC maps were generated: a ZTE derived AC map with a fixed LAC for the bone, an AC map based on the single-atlas approach as provided by the PET/MR manufacturer, a soft-tissue only AC map and, finally, the CT derived attenuation map used as the gold standard (CTAC). All these AC maps were used with different levels of smoothing for PET image reconstruction with and without time-of-flight (TOF). The subject-specific AC map generated by combining ZTE-based segmentation and linear scaling of the normalized ZTE signal into HU was found to be a good substitute for the measured CTAC map in brain PET/MR when used with a Gaussian smoothing kernel of 4 mm corresponding to the PET scanner intrinsic resolution.

As expected TOF reduces AC error regardless of the AC method. The continuous ZTE-AC performed better than the other alternative MR derived AC methods, reducing the quantification error between the MRAC corrected PET image and the reference CTAC corrected PET image.

Keywords: PET/MRI, attenuation correction, ZTE MRI, PET quantification

S Supplementary material for this article is available online

(Some figures may appear in colour only in the online journal)

1. Introduction

One of the main challenges to get accurate quantitative PET images on hybrid PET/MR systems is to correct for the photon attenuation in the absence of CT and transmission scan. CT signal intensity, expressed in Hounsfield Units (HU), is directly related to tissue density and the linear attenuation coefficients (LAC or μ expressed in cm^{-1}) are computed at 511 keV using a bilinear relationship (Carney *et al* 2006). In contrast, the MR signal depends on proton density and relaxation times; it offers a good soft tissue contrast but does not correlate with tissue electron density. Hence, MR-based attenuation correction methods (MRAC) are needed for brain PET/MR.

Several MRAC methods were suggested in the literature for brain imaging to generate a CT surrogate (pseudo-CT) from MR images and derive an attenuation map. The attenuation map can be estimated using the single atlas approach by registering a single average CT template to the MR images acquired with a two-point Dixon pulse sequence (Wollenweber *et al* 2013, Sekine *et al* 2016a). This method is commercially available on some PET/MR scanners. However, the single atlas approach was outperformed by the multi-atlas approach (Sekine *et al* 2016b). The latter is based on a database of CT and corresponding MR images (Burgos *et al* 2014, Mérida *et al* 2017). After registering MR images from the database to the measured T_1 or T_2 weighted MR images, weights were assigned to each CT based on a similarity metric to the measured MR image. The pseudo-CT was then generated by combining the corresponding CT images of the database with the different weights or probabilities. Atlas-based methods show limitations when applied to unusual patient anatomies such as post-operative patients with deformed skull or neurological clips, children with different skull anatomy and density and preclinical applications. Also, these methods are computationally demanding (Sekine *et al* 2016b) and are highly dependent on the registration quality.

Another family of MRAC methods, referred to as segmentation based methods, consists in segmenting images in different tissue classes and assigning a fixed attenuation coefficient to each tissue class (Martinez-Möller *et al* 2009). In Keereman *et al* (2010) and Cabello *et al* (2015), an Ultra-short Echo Time (UTE) pulse sequence was used to acquire signals in tissue with short T_2^* such as the skull and to separate bone and air cavity interfaces. Segmented bone was assigned a fixed LAC in Keereman *et al* (2010) whereas in Cabello *et al* (2015), the relaxation rate R_2^* ($R_2^* = 1/T_2^*$) image obtained from the log of the difference between two short T_E images was mapped into a LAC map. The authors used a linear relationship established between R_2^* values and CT density in HU to get continuous attenuation values in bone from the MR image. Nevertheless, due to relatively long T_E ($\approx 100\mu s$) in UTE, the contrast between bone and parts of soft tissue is weak, which makes it difficult to identify bone. Consequently, a two-points T_2^* weighted pulse sequence is needed to clear the intermediate T_2^* structures and isolate bone signal resulting in a longer acquisition time (few minutes (Keereman *et al* 2010)).

The recent development of zero echo time (ZTE) pulse sequences allows to measure MR signals in bone with a single acquisition (Weiger *et al* 2013). From the ZTE images, bone, soft tissue and air were segmented to derive a pseudo-CT which was later used for attenuation correction of the PET image (Wiesinger *et al* 2016, Delso *et al* 2015). Recently, pseudo-CTs with continuous bone density were generated from ZTE image and scaled using a linear relationship between ZTE intensity and CT density in HU (Sekine *et al* 2016c). However, the existence of such a linear relationship has not been yet fully investigated. Moreover, ZTE signal measured with water and fat suppressed projection imaging (WASPI) (Wu *et al* 2003), a ZTE-based sequence, can be accurately correlated to bone density as shown in Cao *et al* (2008) and Huang *et al* (2015). The AC map derived from the ZTE MR yields similar results as CT when correcting for γ photon attenuation in a bone phantom. All these results suggest that an empirical relationship between the ZTE signal and the attenuation map might exist (Khalifé *et al* 2016a).

Currently, all implemented MRAC methods show limitations regarding unusual head anatomy and bone density variations. The single atlas approach might not be able to handle unusual patient anatomies, intra- and inter-subjects bone density variations (Wollenweber *et al* 2013). Regarding the multi-atlas approach, to the best of our knowledge there is no proof that this approach would be able to handle anatomical abnormalities (Burgos *et al* 2014, Mérida *et al* 2017). The advantage of segmentation-based methods is that they should be able to handle unusual patient anatomies (assuming that the different tissue classes are segmented properly). However, assigning a fixed attenuation coefficients to each tissue class might preclude taking intra- and inter-subjects bone density variations into account. Bone density varies in value and distribution, thus considering a single value for bone density as a reference is approximate. Additionally, taking the bone density variation into account (i.e. intra- and inter-subjects bone density variations) in the attenuation map was shown to reduce the bias in PET quantification (Juttukonda *et al* 2015, Ladefoged *et al* 2015). Consequently, this work describes and tests a segmentation-based approach that circumvents these two limitations (abnormal anatomy and bone density variations) using the ZTE pulse sequence (Khalifé *et al* 2016b).

In this paper, we present a generic segmentation-based MRAC method based on the ZTE pulse sequence with the potential to handle intra- and inter-subjects bone density variations and unusual patient anatomy, while keeping the acquisition time of the ZTE acceptable (e.g. $<$1 min 30 s). The paper is organised as follows. In section 2, the segmentation algorithm of the ZTE images to air, soft tissue and bone masks is presented. In order to derive a ZTE-based pseudo-CT map with continuous μ values in the bones, the evaluation of the relationship between the bone voxels intensity in the ZTE images and in the CT images is then described. The performance of the proposed ZTE-based MRAC method for brain imaging is characterised and compared to alternative approaches in section 3 on a cohort of 16 patients that underwent a PET/CT scan followed by a PET/MR examination. The use of the proposed method to a non-human primate study is also presented in section 3. The main features of the presented method are discussed in section 4 before concluding.

2. Methods

In this study, 16 patients (five females, 11 males), aged 65 ± 6 years (mean $\pm$ standard deviation), were included for lung or digestive cancer with no pathology in the head. They were enrolled after being checked for standard MRI exclusion criteria. All subjects provided a written informed consent after a full explanation of the protocol. The study protocol was in accordance with the latest version of the Helsinki declaration and approved by the national ethical committee.

Patients were first scanned about 60 min after [^{18}F]-FDG injection (injected tracer activity of 302 ± 92 MBq) in a PET/CT scanner (Siemens Biograph 6, Knoxville, TN, USA), with their arms up.

CT images were acquired using a whole-body attenuation correction protocol with 3 mm slice thickness and 1.376×1.376 mm^2 in-plane resolution, tube voltage of 110 kV and exposure set to 80 mA with automatic dose modulation. First, head CT was automatically segmented to remove arms and the table that appears in the field of view. The resulting head CT was registered to MR ZTE image using the Optimized Automatic Image Registration 3D method in MIPAV (CIT-NIH, Bethesda, USA) (Jenkinson and Smith 2001). The obtained transformation was an affine registration with 12 degrees of freedom (DoF) by minimizing a cost function based on normalized mutual information. The registered CT was resampled to the ZTE image resolution by means of a trilinear interpolation. The 16 patients CT were analysed to study intra- and inter-subjects bone density variations.

Forty-five minutes after the PET/CT acquisition, patients underwent a PET/MR exam (GE Signa PET/MR, Waukesha, WI, USA) as a part of this clinical protocol. A bed station centred on the head with 3 min PET acquisition was added in the protocol. During the PET acquisition, a two-points Dixon pulse sequence (named LAVA-flex in the manufacturer nomenclature) used as input for the single-atlas approach (Wollenweber *et al* 2013) and a ZTE (zero echo time) pulse sequence were performed on the head using a 24 channel head-neck receive coil. The two-points Dixon acquisition parameters were the same as in Sekine *et al* (2016a) with an acquisition time of 18 s (resolution $1.95 \times 1.95 \times 2.6$ mm^3, 120 slices, field-of-view (FOV) 50×50 cm^2, flip angle of 5°). The ZTE pulse sequence was a silent 3D radial proton-density weighted sequence (Delso *et al* 2015, Wiesinger *et al* 2016) and was acquired in the axial direction with the following acquisition parameters: 150 readout points, 512 spokes, FOV $240 \times 240 \times 256$ mm^3, flip angle 0.8°, bandwidth ±62.5 kHz, number of excitation 4, leading to a final image resolution of $1.6 \times 1.6 \times 1.6$ mm^3 and scan time of 1 min 20 s. The PET acquisition lasted 3 min for the head station. PET sinograms raw data and MR and CT images were stored for offline reconstruction and processing.

2.1. ZTE segmentation

ZTE images were processed using an in-house program for attenuation maps generation and the PET Recon toolbox provided by the PET/MR manufacturer for PET image reconstruction in Matlab (The mathworks inc., Natik, MA, USA). First, the ZTE images were bias-corrected using the ITK N4-bias filter (Tustison *et al* 2010) to homogenise image intensity. The air and soft tissue peaks of the intensity histogram were fitted using a Gaussian function. This led to a clearer separation of the bone and soft tissue intensity as shown in Wiesinger *et al* (2016). However, as the MR image intensity varied between subjects, a normalisation of ZTE intensities was applied such that the air intensity peak was centred at zero, the soft tissue intensity peak was centred at 1 and the bone voxels intensity were the values in between (see figure 1). An air mask was then created by applying a threshold of 0.3 on the normalized ZTE image which is the distance at 3σ from the air peak value of the fitted air Gaussian (figure 1(a)). The distance between the air peak intensity and the soft tissue peak intensity on the histogram depends on the ZTE acquisition bandwidth per pixel (Wiesinger *et al* 2016), which is identical in all subjects. Therefore, the 0.3 threshold is consistent for all normalized images. As dentine contained inside the teeth appears with low intensities on the ZTE images, it might be mistaken for air. Consequently, holes might appear in the teeth after air segmentation. To circumvent this misclassification, the Zubal phantom (Zubal *et al* 1994) was used to approximately

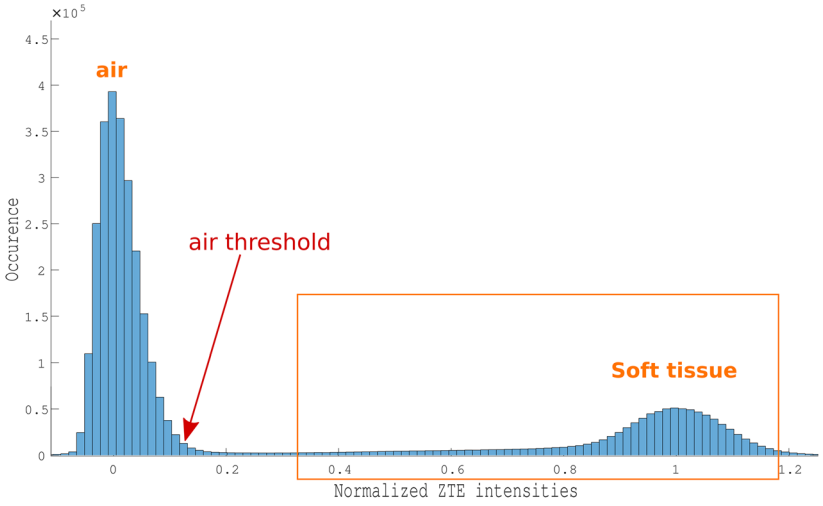

(a)

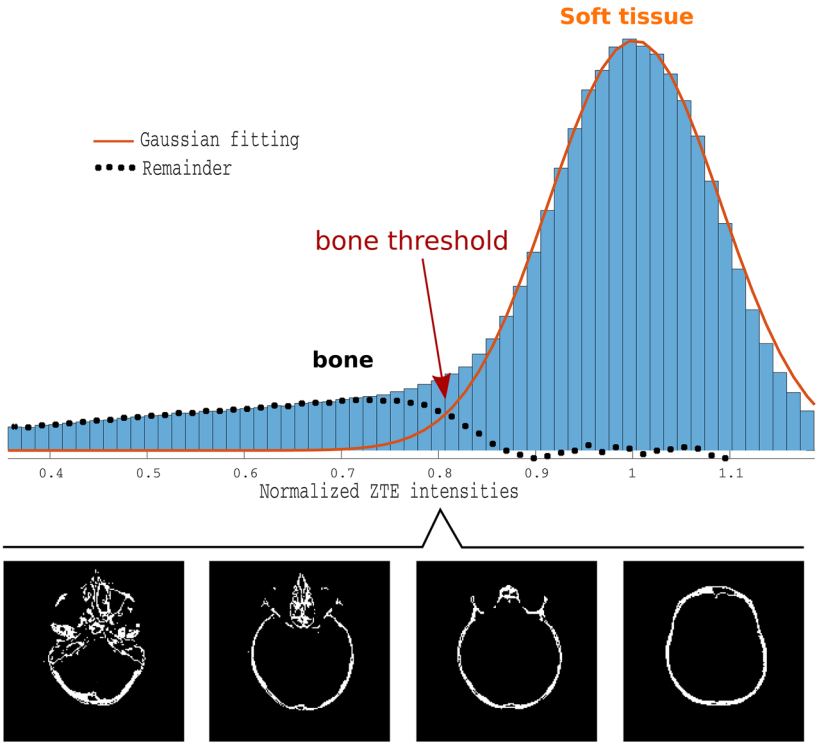

(b)

Figure 1. ZTE images are segmented based on thresholds determined on their histogram. (a) Normalized ZTE intensity histogram. Air threshold is given by the foot of the descending slope of the air peak. (b) Bone intensity threshold is computed by subtracting the soft tissue fitted Gaussian (orange line) from the histogram. The resulting histogram (dotted line) contains the bone information. The threshold used to create a bone mask is the intersection of the two curves as indicated on the figure. The resulting bone mask is shown below at four different slice locations.

locate teeth position in the ZTE image. The Zubal template was registered to the ZTE image using an affine registration with 12 DoF in MIPAV. The volume of the intersection between the teeth mask of the registered Zubal phantom and the air mask created from the ZTE image was considered as bone.

The bone intensity is obtained by subtracting the soft tissue fitted Gaussian from the normalized histogram after removal of the air peak. The remaining intensities in the histogram are then the ones corresponding to the bone voxels and their intersection with the soft tissue fitted Gaussian was used to define the bone voxels threshold (see figure 1(b)). This result is a segmented skull image. Some morphological operations (watershed and opening-closing operations) were applied to remove isolated false positive voxels, if any.

Furthermore, a partial volume effect in the nasal area often yields to a misclassification of soft tissue into bone. Structures in these regions cannot be resolved with the MRI spatial resolution used in this work and the three tissue class intensities overlap in the same voxels leading to bone-like intensities although they contain a mixture of soft issue, air and cartilage. To correct for this, a volume of interest (VOI) is defined around the sinus and the nasal cavities as follows (see supplementary figure 1 (stacks.iop.org/PMB/62/7814/mmedia)): the FOV is divided in two equal parts in the Y (left/right) direction and in 3 equal parts in the X (anterior/posterior) and Z (superior/inferior) directions; the VOI is defined as the intersection of the last third in the Z direction, the middle third in the X direction and the upper half of the Y direction. A different threshold is applied in this VOI to correct for the partial volume effect and remove the misclassified voxels from the bone mask. This local threshold is defined on the histogram as 50% of the intensity at the intersection between the horizontal axis and the tangent line of the curve part lying between 10% and 30% of the soft tissue peak value. After applying this second threshold, the identified voxels are transferred from the bone mask to the soft tissue mask (figure 2).

Finally, the soft tissue mask includes the voxels not assigned to neither the air nor the bone masks.

2.2. ZTE bone attenuation scaling

As shown in earlier studies (Cao *et al* 2008, Huang *et al* 2015), MR ZTE signal intensity measured with a WASPI pulse sequence (water and fat suppressed ZTE (Wu *et al* 2003)) on a bone sample correlates with bone density. In this work, we tested *in vivo* the existence of a relationship between the ZTE signal acquired with a ZTE pulse sequence on the bone and the bone density measured in HU on the CT images in our patients database. Moreover, a linear relationship has been previously used for the conversion of ZTE intensity to density in HU (Sekine *et al* 2016c, Leynes *et al* 2017), but it has not been explicitely given nor precisely justified. To identify an appropriate relationship, a 2D joint histogram was created between the bone CT intensities and the normalized ZTE image intensities rebinned in 256 bins for the 16 patients. Bone voxels were selected on both images (i.e. CT and ZTE) if they met these two conditions:

- voxels have bone-like densities on the CT meaning their densities are within [300, 2000] HU. The maximum CT density was set to 2000 to exclude tooth filling artefacts.
- their 8 neighbours in 2D for every slice fulfil the previous criterion.

The 8 neighbourhood in 2D was used instead of the 26 neighbourhood in 3D because the latter would be very conservative in the case of the skull spherical geometry. To determine this relationship, we applied a principal component analysis (PCA) (Abdi and Williams 2010) on the joint histograms of the 16 patients. The first principal component (PC) explains the largest variance of the histograms and the second PC explains the second largest variance while being

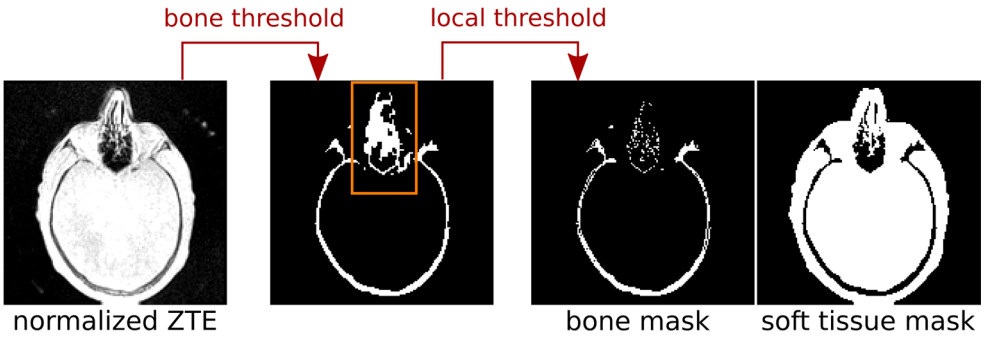

Figure 2. To correct for the partial volume effect in the nasal cavities, a different threshold is applied on the VOI defined on the image. The false positive voxels are removed from the bone mask and transferred to the soft tissue mask.

orthogonal to the first PC. A leave-one-out (LOO) cross validation was applied on the 16 datasets to evaluate the accuracy of the model prediction. At each iteration, one joint histogram was pulled out for testing and the 15 remaining joint histograms were used for computing the model. The model was estimated using the first PC given by PCA of the grouped 15 joint histograms and tested against the first PC of the remaining subject. The coefficient of determination R^2 between the predictions and the data from which the model was used to assess the quality of the prediction. This was repeated for each joint histogram of the 16 patients.

A relationship was determined by linear regression applied on the prediction of the first PC of the 16 patients. The sensitivity of the relationship to the CT-ZTE registration accuracy was evaluated by shifting the CT image by one voxel in the six 3D directions.

2.3. PET quantification

2.3.1. AC map generation. Five attenuation maps were created to correct the brain PET emission data. The reference attenuation map was derived from the CT image, using the bilinear relationship to convert HU into LAC values (Carney *et al* 2006), after having registered and rescaled the CT image to the ZTE image. The 'atlas-based' attenuation map was the one generated using the PET/MR built-in reconstruction algorithm. It used the acquired In-Phase Dixon image, usually acquired to distinguish water and fat tissues, to which a mean single-atlas CT-based attenuation map is registered. The 'atlas-based' attenuation map was spatially filtered with a default Gaussian kernel of 10 mm by the built-in reconstruction algorithm before the PET image reconstruction.

The ZTE images segmented using the three classes based on their attenuating property were converted into an AC map as follows: the air class was set to -1000 HU equivalent to a LAC of 0 cm^{-1} by definition and the soft tissue class was set to 31.58 HU equivalent to a LAC of 0.098cm^{-1} at 511 keV based on our CT to LAC scaling at 110 kV. For the bone class, three cases were investigated:

- fixed bone attenuation 'ZTE fixed': in which the bone density was set to 1136 HU corresponding to a LAC of 0.151 cm^{-1} at 511 keV (Keereman *et al* 2010).
- continuous bone attenuation 'ZTE cont': An AC map was created by scaling bone voxels in the ZTE image using the relationship established between normalized ZTE intensity and CT density in HU as explained earlier.

- no bone attenuation 'no bone': An AC map ignoring the bone in the segmented ZTE image by assigning the soft tissue attenuation value (i.e. 0.098 cm^{-1}) to the bone voxels.

The resulting AC maps are the following:

- atlas: the vendor atlas-based AC map with default 10 mm spatial smoothing
- CT: CT-based AC map without smoothing
- ZTEfixed: segmented ZTE-based AC map with constant bone LAC without smoothing
- ZTEcont: segmented ZTE-based AC map with continuous bone LAC without smoothing
- nobone: segmented ZTE-based AC map ignoring bone attenuation without smoothing

2.3.2. Spatial smoothing. As shown in Meikle *et al* (1993), mismatched spatial resolutions between the attenuation map and the emission data might cause attenuation artefacts. Therefore, we studied the effect of a 3D isotropic spatial Gaussian smoothing of the AC maps on the PET image. Besides the original AC map resolution, the FWHM of 4 mm was chosen to match the PET/MR intrinsic resolution as the attenuation map should match the resolution of the emission data in the projection space regardless of the reconstruction algorithm (FBP or OSEM). The FWHM of 10 mm was the default blurring applied on the AC map by the vendor. The atlas-based AC map is used with a 10 mm smoothing to assess the vendor-provided method. The suffixes 'filt4' and 'filt10' are added to each AC map name to indicate 4 mm smoothing and 10 mm smoothing respectively.

2.3.3. TOF contribution. TOF information in the reconstruction reduces the sensitivity to inconsistencies in the attenuation correction (Conti 2010). Since not all PET/MR scanners are equipped with the TOF technology, AC methods should be compared on non-TOF and TOF reconstructions to estimate the error introduced by the AC map independently of the PET detectors performance. All images with the different AC maps were thus reconstructed twice: once with and once without TOF information.

In addition, all attenuation maps were resliced to a slice thickness of 2.78 mm to match the PET emission data space. PET images were reconstructed using an OSEM (respectively with and without TOF) algorithm with 8 iterations, 28 subsets, voxel size $1.17 \times 1.17 \times 2.78$ mm^3, PSF modelling, attenuation correction, scatter correction and no post-filtering, as suggested by the manufacturer for brain images.

In total, for each of the 16 patients, 22 PET images were reconstructed using 11 different AC maps and 2 TOF options (on/off).

2.3.4. Primate application. One of the limitations of using an atlas-based AC is non-human primate application. As the ZTE-based AC approach aims at providing a subject-specific AC map, its application to primates would illustrate its flexibility. We thus included an adult baboon subject in this study. The animal was anaesthetized using isoflurane and injected with 88 MBq of ^{18}F-FDG before undergoing a PET-CT scan followed by a PET-MR scan using the same protocol as described earlier. A ZTE pulse sequence with the same parameters as given before was acquired on the head station. Three AC maps ZTEfixed, ZTEcont and nobone were generated as previously described and the PET images were reconstructed using the 3 AC maps and the CTAC map smoothed with a 4 mm FWHM Gaussian kernel and the TOF-OSEM algorithm.

2.4. Image analysis

All reconstructed PET images were registered and spatially normalized to a PET brain template in montreal neurological institute (MNI) space using SPM12 (University College London). The registered and normalized images were resampled to $2 \times 2 \times 2$ mm^3.

A quantitative analysis was performed to evaluate the MRAC methods with respect to the CTAC reference method. The reference CTAC and the compared MRAC images were chosen with the same spatial blurring. The atlas corrected image whose AC map is blurred with 10 mm Gauss kernel was compared to all 3 CTAC images (no blurring, 4 mm and 10 mm filters). The comparison was performed for each TOF and non TOF reconstructions as follows: 'atlas-CT', 'nobone-CT', 'ZTEfixed-CT', 'ZTEcont-CT', 'atlas-CTfilt4', 'nobonefilt4-CTfilt4', 'ZTEfixedfilt4-CTfilt4', 'ZTEcontfilt4-CTfilt4', atlas-CTfilt10', 'nobonefilt10-CTfilt10', 'ZTEfixedfilt10-CTfilt10', 'ZTEcontfilt10-CTfilt10'. [18F]-FDG being a glucose analog, its main uptake is in grey matter. Consequently, a grey matter mask defined in MNI space from a PET template was applied. The relative difference image in % in grey matter is given by :

$$\mathrm{Diff}_{\mathrm{MRAC-CTAC}}(\%) = 100 \cdot \frac{I_{\mathrm{MRAC}} - I_{\mathrm{CTAC}}}{I_{\mathrm{CTAC}}}$$

where I_{MRAC} is the PET image corrected with one of the MRAC methods, and I_{CTAC} is the PET image corrected with the gold standard reference CTAC.

Furthermore, a ROI analysis using the automated anatomical labelling (AAL) brain atlas with 116 regions of interest (ROI) (Tzourio-Mazoyer *et al* 2002) was performed to assess the PET uptake difference in various brain regions. The 116 ROI were grouped into eight brain regions: frontal, parietal, occipital, parietal, insula and cingulate, central, temporal, cerebellum. Only grey matter voxels were considered for the eight brain ROI. Relative difference and standard error were computed in each ROI between the compared MRAC image and the CTAC image and averaged over the 16 patients. A voxelwise relative difference image was displayed between the MRAC corrected images and the CTAC corrected image to visually assess the location of the differences between the MRAC methods to the reference method. Finally, the root mean square error (RMSE) was computed in grey matter between MRAC images and CTAC images to measure the global performance of the methods. A paired t-test was applied to evaluate the influence of TOF on the global error.

3. Results

All CT, Dixon and ZTE images were visually inspected to check that they did not include artefacts.

3.1. ZTE segmentation

The segmentation algorithm based on the ZTE image histogram Gauss fitting step, intensity normalisation and bone intensities identification performed visually well in all patients. The air-bone interface is well segmented in the sinus, nasal and the spheroid cavities as well as in the airways. The segmented maps are visually in good agreement with the corresponding CT images (see figure 3 for three examples of pseudo-CTs together with the corresponding CT). Spongious temporal bones and cartilage in the nasal structures can be misclassified as soft tissue or air due to their ZTE intensity closer to soft tissue or because of partial volume effect. Differences can be seen around the neck regions due to different positioning of the patients in the PET/CT and PET/MR scanners that was not compensated for by our registration procedure, but this region had little impact on the reconstructed brain region.

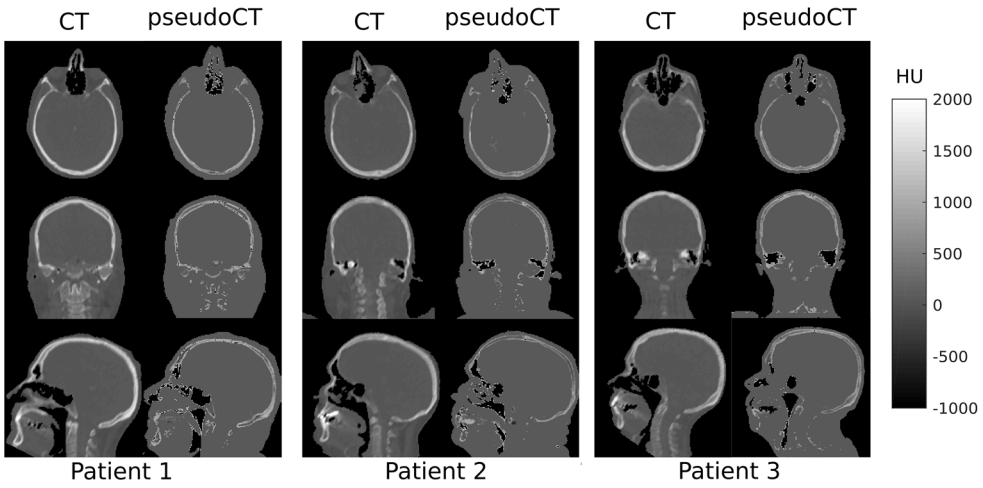

Figure 3. Three examples of CT images and ZTE-based pseudo-CTs generated using the segmentation algorithm and the linear relationship between normalized ZTE intensity and CT density in HU.

3.2. ZTE bone attenuation scaling

Over the 16 patients, observing CT density in the head bone (figure 4) showed that:

(i) bone density in HU changes in the same patient between low density cancellous (200–300 HU) bone and cortical bone (>1100 HU);
(ii) Median bone density varies between 500 HU and 800 HU over the 16 patients suggesting the need for patient-dependent bone attenuation values.

A relationship between CT HU and ZTE acquired with the parameters described earlier was visually observed on the joint histogram (figure 5). The PCA of the ZTE and CT joint histograms of all the patients showed that 60% of the variance is described by the first PC. The first PC allowed us to determine a linear relationship between normalized ZTE intensities and CT densities in HU. The LOO cross-validation showed that all predicted first PC from any other 15 training PCs are in very good agreement and have a coefficient of determination of 0.92. The linear regression of the predicted PCs (the direction vectors of the first PC) yielded a relationship within a tight 95% confidence interval (figure 6) given by:

$$\mathrm{CT(HU)} = -1182 \times ZTE_{\mathrm{norm}} + 1393.$$

Using this relationship, the coefficient of determination R^2 between the predictions and the real data was 0.92. The error on the linear fitting after shifting the CT by a voxel in six 3D directions was not significant: slope $= -1146 \pm 42$, intercept $= 1387 \pm 18$. The goodness of fit was $R^2 = 95.5 \pm 0.6$. The linear relationship between normalized ZTE intensity and CT density in HU was applied on all segmented ZTE images to generate an AC map for PET reconstruction. The generated AC map respected the variations in bone density of the previously segmented ZTE image.

Additionally, the bone density distributions of the pseudo-CT generated with the continuous ZTE derived method and the CT are displayed in figure 4 showing that the continuous ZTE pseudo-CT was able to capture a large part of the intra- and inter-subject variability. The coefficient of determination R^2 computed from the linear regression of the joint histograms

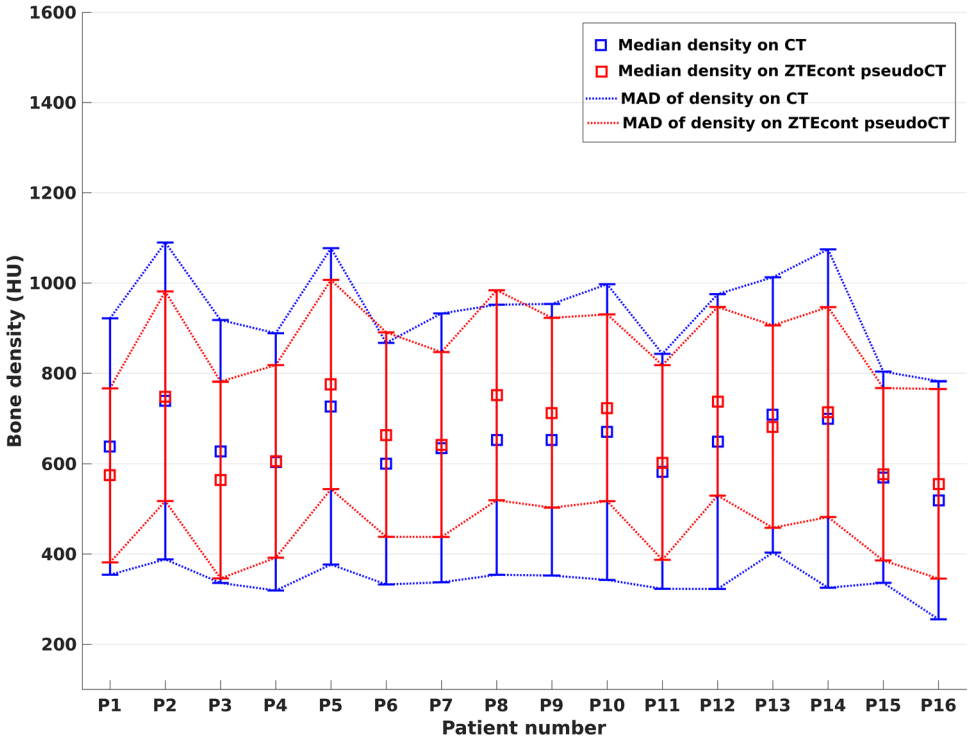

Figure 4. Bone density distribution in HU observed in CT (in blue) and continuous ZTE pseudo-CT (in red), represented by median value ± median absolute deviation (MAD). The displayed values were obtained from unsmoothed CTs and pseudo-CTs.

between the pseudo-CTs and the reference CT to estimate their similarity was of 0.16 for nobone, 0.33 for atlas, 0.24 for ZTEfixed and 0.67 for ZTEcont.

3.3. PET quantification

All PET images were reconstructed successfully with all the AC maps using TOF and non-TOF OSEM. The global performance of all methods in the grey matter is depicted in figure 7 for non-TOF and TOF reconstructions. It showed that the RMSE in grey matter in 16 patients is overall less than 2%. Nobone-AC and atlas gave the highest RMSE, the biggest variability and the highest number of outliers. All ZTE-based AC had a RMSE lower than 0.5% and low variability. ZTEcont-AC gave the lowest RMSE and the lowest variability regardless of the usage of TOF or of the smoothing size of the AC map, with outliers when using a 10 mm Gaussian kernel for smoothing. RMSE computed for non-TOF reconstructions was significantly higher than the one for TOF reconstructions ($p < 10^{-3}$).

3.3.1. Relative difference. Figures 8(a) and (c) depict the relative difference maps between all the MRAC reconstructions and the CTAC reference reconstruction. They showed that PET images reconstructed with no bone MRAC underestimate CTAC image with errors reaching −25% without TOF and −17% with TOF in a circular region near the cortical bone. This region grows larger as the smoothing kernel increases (figures 8(a), (c) and 9).

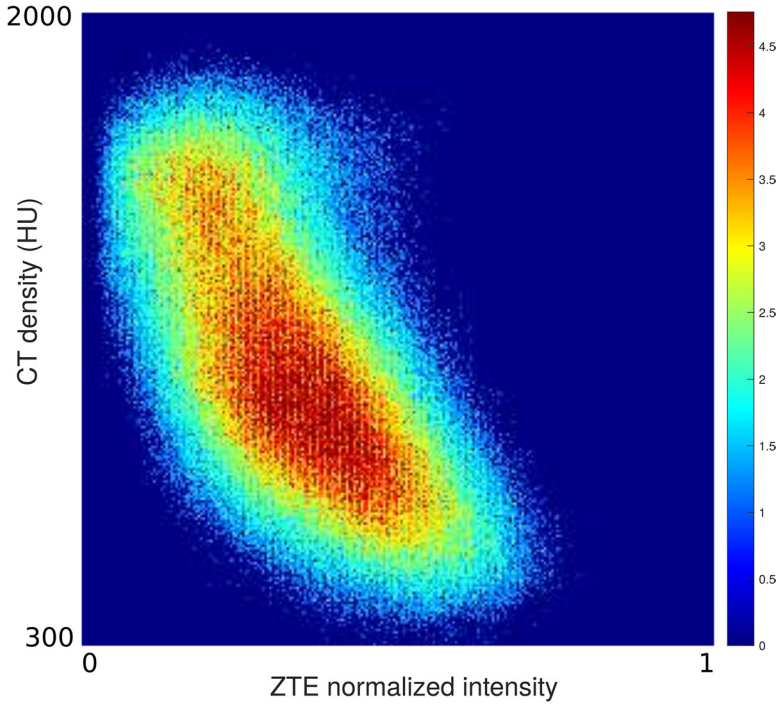

Figure 5. The joint histograms of CT and normalized ZTE including all patients. The X and Y axis coordinates of the joint histogram are respectively the normalized ZTE image intensity between $[0, 1]$ and the CT density between $[300, 2000]$ HU. The Z coordinate is the number of voxels having the combination of intensities (X, Y).

Conversely, PET images reconstructed with the atlas-based AC showed an overestimation of CTAC images on the whole brain that reaches $+12\%$ without smoothing and reduces as the smoothing kernel increases because the resolution mismatch decreases. A left-right asymmetry was observed on atlas-AC images suggesting a registration bias. The error remained the largest in the parietal region of the brain (figure 9). Additionally, the atlas-based correction showed the highest variability regardless of the filter FWHM and the use of TOF as reflected by the high standard deviation on all slice locations in figures 8(b) and (d).

ZTE-based AC maps, whether with a fixed bone LAC or a continuous one, yielded an overall error on PET images between -5% and $+5\%$ with respect to CTAC images and a low variability with all smoothing filters and reconstructions (figure 8). Fixed ZTE-AC showed most often a positive error whereas continuous ZTE-AC showed a negative error except for the temporal lobe and the cerebellum. As shown in figure 9, continuous ZTE and fixed ZTE performed similarly in frontal, occipital, parietal and central regions with 4 mm filtering but continuous ZTE outperformed fixed ZTE in the insula and cingulate, temporal and the cerebellum regions for all reconstructions. Temporal lobes close to temporal bones showed an overestimation on the ZTE-based AC images (fixed and continuous) with all smoothing filters.

3.3.2. Primate application. The continuous ZTE AC map of the baboon is displayed in figure 10. It showed a good agreement in bone depiction and HU scaling with CTAC. Affine registration showed some limitations at the neck area because the head position was different in the PET/CT and in the PET/MR. The spine was slightly misaligned on the registered

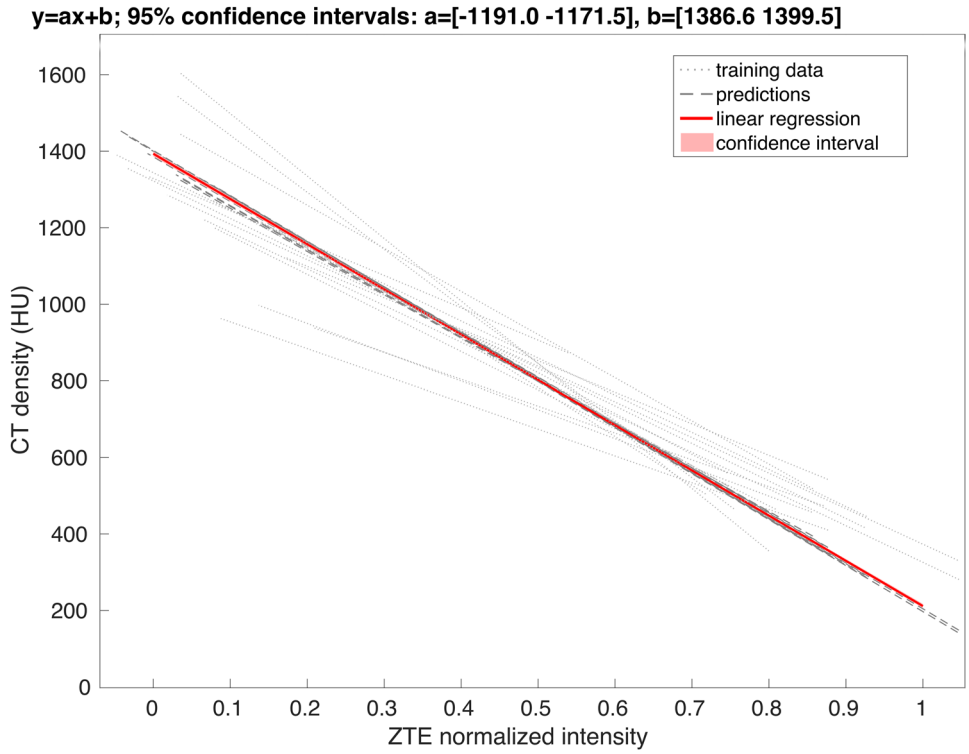

Figure 6. Linear relationship between normalized ZTE intensity and CT density in HU. The linear regression (red line) fits the first PC predicted by LOO cross-validation on the 16 patients joint histograms ($R^2 = 92.19\%$).

CT with respect to the ZTE image but this did not impact the skull registration. The reconstructed PET images corrected using MRAC were compared to CTAC and the relative mean error $\pm$ standard deviation computed on the grey matter were: $-6.4 \pm 7.4\%$ for nobone, $4.8 \pm 6.2\%$ for ZTEfixed, $1.0 \pm 6.0\%$ for ZTEcont. RMSE values were 2.14% for nobone, 1.65% for ZTEfixed and 1.26% for ZTEcont.

4. Discussion

We have presented a ZTE MRI-based method to generate a pseudo-CT mimicking bone density in the skull. The proposed approach is close to that described by Sekine *et al* (2016c) but differs in three main aspects: (1) the spatial resolution of the ZTE image (2.4 mm versus 1.6 mm in our method), (2) the segmentation algorithm used to identify the bones from the ZTE image, (3) the method used to derive the CT—ZTE signal relationship. We have shown the reproducibility of this method in 16 patients while comparing it to the measured CT attenuation map in terms of regional activity in the attenuation corrected PET images. The segmentation algorithm performed well in separating bone, air cavities and soft tissue. It suffered from partial volume effect in the nasal sinus area. Small structures of bone, air and soft tissue coexist in this area and the chosen MRI resolution does not allow to recover entirely these structures in the segmented AC map. To avoid false positive in bone mask, a lower segmentation threshold was set in this area. This adds an extra condition dependent

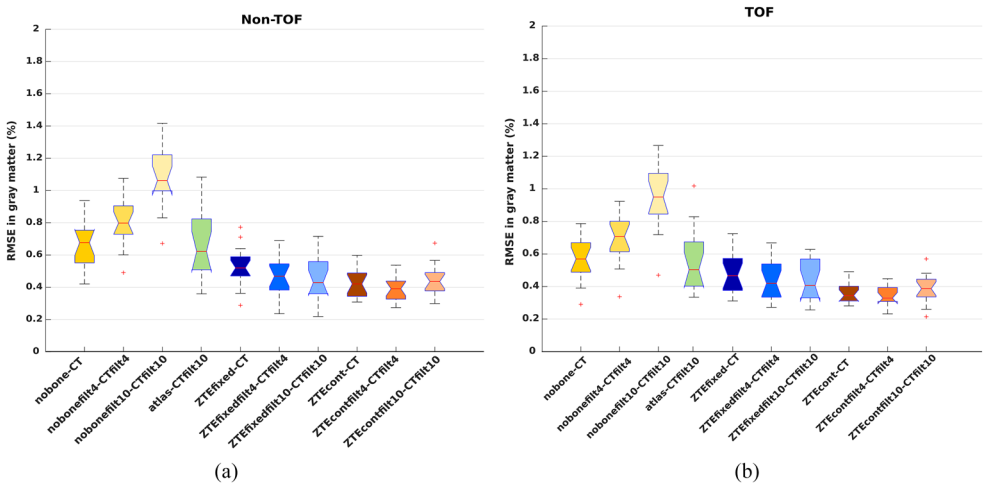

(a) (b)

Figure 7. Global performance of all AC methods in the 16 patients in grey matter based on root mean square error (RMSE). The red line represents the median, the box contains the 25th and 75th percentiles, the whiskers show one interquartile range (IQR) and the red ' + ' show the outliers. The RMSE is computed between the reconstructed PET images using the MRAC methods and the CTAC (the gold standard). The upper graph shows the errors for non-TOF reconstructions and the lower one is for TOF reconstructions.

on the localisation of the head in the field of view. In addition, spongious and cortical bones show ZTE intensities closer to soft tissue and can be misclassified using the threshold set for the bone mask, which is the case in the temporal bones, the thick skull bone in the back of the head and teeth. The second is recovered by morphological transformations and the latter relies on an *a priori* extracted from a registered Zubal template. However, the segmentation could probably be improved in the nasal and dental area by using more sophisticated segmentation algorithms (Ma *et al* 2010, Sharma and Aggarwal 2010) in addition to the presented histogram-based algorithm.

A single CT with the same bone densities is unlikely to generate an accurate AC map that represents all patients. Continuous skull bone densities were modelled and scaled for each patient using a relationship between normalized ZTE intensities and CT density in HU. With the ZTE to CT scaling relationship, intra and inter-subjects bone density variability was successfully taken into account. The continuous ZTE AC map was a good substitute to CT-based attenuation map as it is reflected by the low standard deviation of the error on the ZTE-based MRAC with respect to CTAC as opposed to higher error variability in the atlas-based MRAC images. However, this relationship is valid only for the described ZTE acquisition parameters and for CT Xray energy corresponding to 110 kVp. If changed, the ZTE image resolution and pixel bandwidth might impact the ZTE intensity and modify the relationship. We also checked that an error in CT to ZTE registration did not significantly affect the relationship and the goodness of the fit, suggesting that the relationship is robust enough with respect to possible registration errors.

Further, to make this relationship even more robust and reliable, a larger database should be considered to account for various bone densities, ages and skull thicknesses. This would allow to test the validity of this relationship on a broader population of subjects. Nonetheless, the linear relationship applied to our 16 patients database yielded a good agreement between

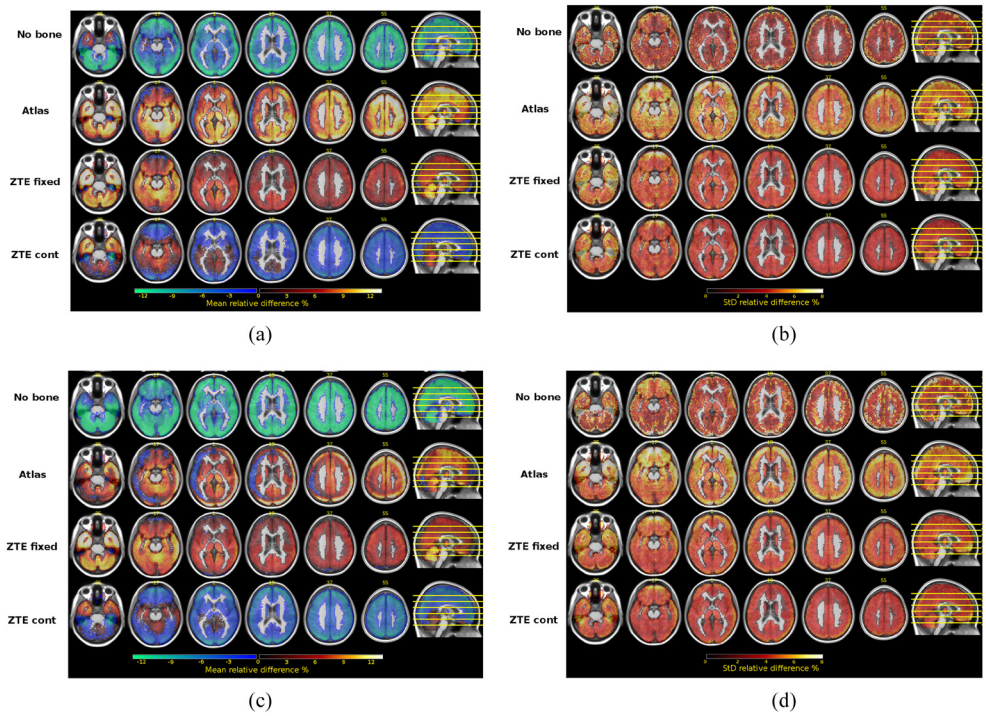

Figure 8. Relative difference maps (left) and standard deviation maps (right) between the TOF reconstructions using CTAC as reference, averaged over the 16 patients. AC maps were smoothed before reconstruction with: ((a), (b)) 4 mm FWHM Gaussian kernel, ((c), (d)) 10 mm FWHM Gaussian kernel.

CTAC and ZTE-AC PET images. This relationship was also successfully applied to a primate subject to generate a ZTE-based AC map that was in good agreement with the corresponding CT. The results obtained on the baboon are consistent with the results obtained on the human data as nobone underestimates the CTAC reference uptake, ZTEfixed overestimates it and ZTEcont has a low overestimation of the uptake. As a result, the relationship determined on an adult human database is not specific to this database but can be used for other human subjects and even primates.

Continuous ZTE AC showed the best performance when studying the RMSE on grey matter even if all methods presented a RMSE less than 2%. However, the effect of attenuation correction is not homogeneous over the whole brain, it is larger in the cortex closer to the skull while it gets smaller towards the centre of the brain (Andersen *et al* 2014). Consequently, a global RMSE on the whole brain uptake shows an overall performance of the AC method but does not reflect the spatial variation of the error in the brain. As a result, ignoring the bone in the AC map did not lead to a significantly higher error than the other methods. However, the pixelwise relative difference map demonstrates spatial bias of each AC method. The misclassification of temporal bones or nasal cavities on the ZTE-AC map leads to a localized high error in the temporal lobe, as reported also in Sekine *et al* (2016c). As temporal bones are hollow bones that contain air holes, it is difficult to separate them from air in the ZTE image. In some cases, the segmentation algorithm classifies them as air (see for example patient 3 in figure 3) leading to this uptake underestimation in the temporal poles.

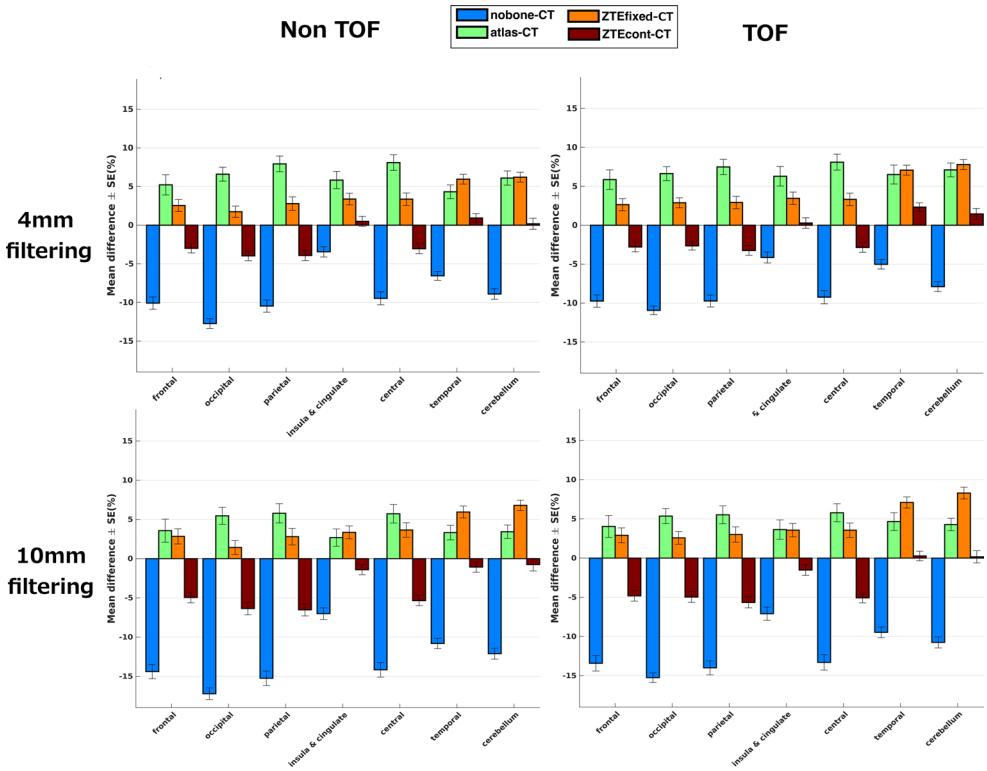

Figure 9. Relative difference in % ± standard error (SE) in regions of the brain between an MRAC image and CTAC image, averaged over the 16 patients. The AC maps used in the first row were smoothed with a 4 mm FWHM Gaussian kernel and in the second row were smoothed with a 10 mm FWHM Gaussian kernel. The first column contains the non-TOF reconstructions and the second column contains the TOF reconstructions.

An asymmetrical left-right error distribution was also observed in the atlas-AC difference map that might be due to a registration bias of the CT template to the low resolution Dixon-MRI.

The standard single-atlas attenuation correction method was compared to the proposed ZTE-based method to study its accuracy in different patients using the acquired CT as a gold standard. PET images corrected based on the atlas overestimated the values in the PET images corrected with CTAC. This result is in contradiction with previous published results (Sekine *et al* 2016c) that used a similar ZTE pulse sequence and the same PET/MR scanner. Sekine *et al* (2016c) reported that PET images corrected with atlas underestimate PET images corrected with CTAC. This opposite conclusion can be due to several factors: the difference in the ZTE image resolution and in the segmentation algorithm implementation, the difference in the CTAC used as a reference or the difference in the linear attenuation coefficient scaling relationship.

Since the atlas derived pseudo-CT was smoothed with a 10 mm FWHM, we have applied a spatial smoothing of 4 mm and 10 mm FWHM on the AC maps generated from CT and ZTE and used the resulting maps to correct PET images. This allowed determining the impact of spatial smoothing of the AC map on the PET image. Increasing the smoothing kernel width increased the error for all AC maps except for the atlas. This is explained by the original

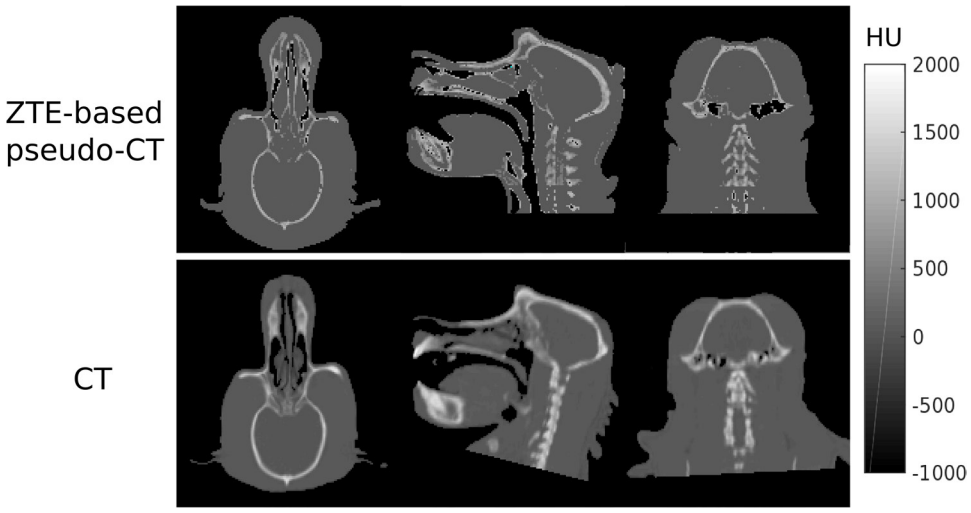

Figure 10. Pseudo-CT generated from ZTE image on the baboon subject and the registered CT. The rigid registration failed in the neck area because of the difference of the head position between the PET/CT and the PET/MR scans.

filtering applied to atlas AC map; applying the same smoothing filter width on the CTAC leads to a better match between both AC maps. However, 4 mm FWHM is the size needed to match the intrinsic PET resolution and has been commonly used in similar studies (Ladefoged *et al* 2017). Atlas-AC is smoothed with a 10 mm FWHM kernel to reduce patients variability as it is made from an average CT template. This is one of the limitation of the atlas-based method. Furthermore, an excessive smoothing of the AC map leads to a mismatch in resolution causing attenuation artefacts (Meikle *et al* 1993).

The contribution of TOF was evaluated. PET quantification errors with non-TOF reconstructions were significantly higher than the errors with TOF reconstructions as revealed by a paired t-test (details in the results section), in agreement with other recent studies (Conti 2010, Mehranian A and Zaidi H 2015, Delso *et al* 2017).

As for AC methods variability, the atlas method presented the highest inter-patient error standard deviation to the mean relative difference map (figures 8(b)–(d)). ZTE-based methods (fixed and continuous) both showed a low error standard deviation to the mean relative difference map. This demonstrates that ZTE-based methods have a similar performance as the CT-based methods across all patients.

These results could be compared to the multi-atlas algorithm as the multi-atlas approach was shown to present a slightly lower error than the single-atlas approach when compared to CTAC especially in brain region located close to the skull (Sekine *et al* 2016c). A study conducted on a large cohort to compare different MRAC methods (Ladefoged *et al* 2017) reported that multi-atlas presented outliers, explained by the bone density that could be over or underestimated when using a CT database and by registration errors. Registration is not an issue in ZTE-based MRAC since the MRI and the PET images are acquired simultaneously and the head is constrained by the coil. Additionally, scaling bone density from MR measured intensity ensures a patient-specific density in the AC map as was shown in a similar study using R_2^* based AC maps (Juttukonda *et al* 2015). Therefore, even though multi-atlas is a promising method, ZTE MRI might prove to be a more robust and adaptive method for attenuation correction. It can potentially be easier to extend to paediatrics, non-human primates and post-operative applications.

5. Conclusion

In this work, an MRAC method based on ZTE was presented and compared with several alternatives. It is demonstrated that ZTE MRI combined with the linear scaling is a good candidate to produce a pseudo-CT for attenuation correction in PET/MR brain imaging. It led to a more accurate and more reproducible performance than that of single atlas algorithm in our cohort of 16 patients. In addition, it was used to generate an accurate AC map for a primate subject. The method handles intra- and inter-patient bone density variation and abnormal anatomy. The ZTE acquisition is silent and lasts less than one and a half minutes making it especially appealing for delicate subjects such as children. The attenuation map is generated within few minutes of post-processing which makes it applicable to standard brain PET/MR protocols.

Acknowledgments

This work was supported by a public grant overseen by the French National Research Agency (ANR) as part of the 'Investissement d'Avenir' program, through the 'Lidex-PIM' project funded by the IDEX Paris-Saclay, ANR-11-IDEX- 0003-02. This work was performed on a platform of France Life Imaging network partly funded by the grant ANR-11-INBS-0006. The authors would like to thank GE Healthcare for providing access to research tools and prototype pulse sequences, Michaël Czisch, Victor Spoormaker and Philipp Sämann for providing the high resolution 3D-T1w template and Hervé Abdi for the valuable discussion on PCA.

References

Abdi H and Williams L J 2010 Principal component analysis *Wiley Interdiscip. Rev. Comput. Stat.* **2** 433–59

Andersen F L, Ladefoged C N, Beyer T, Keller S H, Hansen A E, Højgaard L, Kjær A, Law I and Holm S 2014 Combined PET/MR imaging in neurology: MR-based attenuation correction implies a strong spatial bias when ignoring bone *NeuroImage* **84** 206–16

Burgos N *et al* 2014 Attenuation correction synthesis for hybrid PET-MR scanners: application to brain studies *IEEE Trans. Med. Imaging* **33** 2332–41

Cabello J, Lukas M, Förster S, Pyka T, Nekolla S G and Ziegler S I 2015 MR-based attenuation correction using ultrashort-echo-time pulse sequences in dementia patients *J. Nucl. Med.* **56** 423–9

Cao H, Ackerman J L, Hrovat M I, Graham L, Glimcher M J and Wu Y 2008 Quantitative bone matrix density measurement by water-and fat-suppressed proton projection MRI (WASPI) with polymer calibration phantoms *Magn. Reson. Med.* **60** 1433–43

Carney J P J, Townsend D W, Rappoport V and Bendriem B 2006 Method for transforming CT images for attenuation correction in PET/CT imaging *Med. Phys.* **33** 976–83

Conti M 2010 Why is TOF PET reconstruction a more robust method in the presence of inconsistent data? *Phys. Med. Biol.* **56** 155–68

Delso G, Khalighi M, Ter Voert E, Barbosa F, Sekine T, Hüllner M and Veit-Haibach P 2017 Effect of time-of-flight information on PET/MR reconstruction artifacts: comparison of free-breathing versus breath-hold MR-based attenuation correction *Radiology* **282** 229–35

Delso G, Wiesinger F, Carl M, McKinnon G, Khalighi M, ter Voert E, Barbosa F, Huellner M and Veit-Haibach P 2015 ZTE-based clinical bone imaging for PET/MR *J. Nucl. Med.* **56** 1806–6

Huang C, Ouyang J, Reese T, Wu Y, El Fakhri G and Ackerman J 2015 Continuous MR bone density measurement using water-and fat-suppressed projection imaging (WASPI) for PET attenuation correction in PET-MR *Phys. Med. Biol.* **60** N369–81

Jenkinson M and Smith S 2001 A global optimisation method for robust affine registration of brain images *Med. Image Anal.* **5** 143–56

Juttukonda M R, Mersereau B G, Chen Y, Su Y, Rubin B G, Benzinger T L, Lalush D S and An H 2015 MR-based attenuation correction for PET/MRI neurological studies with continuous-valued

attenuation coefficients for bone through a conversion from $R2^*$ to CT-Hounsfield units *NeuroImage* **112** 160–8
Keereman V, Fierens Y, Broux T, De Deene Y, Lonneux M and Vandenberghe S 2010 MRI-based attenuation correction for PET/MRI using ultrashort echo time sequences *J. Nucl. Med.* **51** 812–8
Khalifé M, Nioche C, Fernandez B, Buvat I, Soussan M, Desarnaud S and Comtat C 2016a Exploring the relation between MR ZTE intensity and tissue density: application to MR attenuation correction in PET/MR *Proc. IEEE Nuclear Science Symp. and Medical Imaging Conf. (Strasbourg, FR)*
Khalifé M, Soussan M, Desarnaud S, Kallou L, Brulon V and Comtat C 2016b Correcting photon attenuation in brain PET-MR using a ZTE sequence and comparison to CT-based attenuation correction *J. Nucl. Med.* **57** 1871
Ladefoged C N, Benoit D, Law I, Holm S, Kjær A, Højgaard L, Hansen A E and Andersen F L 2015 Region specific optimization of continuous linear attenuation coefficients based on UTE (RESOLUTE): application to PET/MR brain imaging *Phys. Med. Biol.* **60** 8047–65
Ladefoged C N *et al* 2017 A multi-centre evaluation of eleven clinically feasible brain PET/MRI attenuation correction techniques using a large cohort of patients *NeuroImage* **147** 346–59
Leynes A P, Yang J, Shanbhag D D, Kaushik S S, Seo Y, Hope T A, Wiesinger F and Larson P E 2017 Hybrid ZTE/Dixon MR-based attenuation correction for quantitative uptake estimation of pelvic lesions in PET/MRI *Med. Phys.* **44** 902–13
Ma Z, Tavares J A M R S, Jorge R N and Mascarenhas T 2010 A review of algorithms for medical image segmentation and their applications to the female pelvic cavity *Comput. Methods Biomech. Biomed. Engin.* **13** 235–46
Martinez-Möller A, Souvatzoglou M, Delso G, Bundschuh R A, Chefd'hotel C, Ziegler S I, Navab N, Schwaiger M and Nekolla S G 2009 Tissue classification as a potential approach for attenuation correction in whole-body PET/MRI: evaluation with PET/CT data *J. Nucl. Med.* **50** 520–6
Mehranian A and Zaidi H 2015 Impact of time-of-flight pet on quantification errors in mr imaging-based attenuation correction *J. Nucl. Med.* **56** 635–41
Meikle S R, Dahlbom M and Cherry S R 1993 Attenuation correction using count-limited transmission data in positron emission tomography *J. Nucl. Med.* **34** 143–50
Mérida I, Reilhac A, Redouté J, Heckemann R A, Costes N and Hammers A 2017 Multi-atlas attenuation correction supports full quantification of static and dynamic brain PET data in PET-MR *Phys. Med. Biol.* **62** 2834–58
Sekine T, Buck A, Delso G, ter Voert E E, Huellner M, Veit-Haibach P and Warnock G 2016a Evaluation of atlas-based attenuation correction for integrated PET/MR in human brain: application of a head atlas and comparison to true CT-based attenuation correction *J. Nucl. Med.* **57** 215–20
Sekine T *et al* 2016b Multi-atlas—based attenuation correction for brain 18F-FDG PET imaging using a time-of-flight PET/MR scanner: comparison with clinical single-atlas—and CT-based attenuation correction *J. Nucl. Med.* **57** 1258–64
Sekine T, ter Voert E E, Warnock G, Buck A, Huellner M, Veit-Haibach P and Delso G 2016s Clinical evaluation of zero-echo-time attenuation correction for brain 18F-FDG PET/MRI: comparison with atlas attenuation correction *J. Nucl. Med.* **57** 1927–32
Sharma N and Aggarwal L M 2010 Automated medical image segmentation techniques *J. Med. Phys.* **35** 3–14
Tustison N J, Avants B B, Cook P A, Zheng Y, Egan A, Yushkevich P A and Gee J C 2010 N4ITK: improved N3 bias correction *IEEE Trans. Med. Imaging* **29** 1310–20
Tzourio-Mazoyer N, Landeau B, Papathanassiou D, Crivello F, Etard O, Delcroix N, Mazoyer B and Joliot M 2002 Automated anatomical labeling of activations in SPM using a macroscopic anatomical parcellation of the MNI MRI single-subject brain *NeuroImage* **15** 273–89
Weiger M, Stampanoni M and Pruessmann K P 2013 Direct depiction of bone microstructure using MRI with zero echo time *Bone* **54** 44–7
Wiesinger F, Sacolick L I, Menini A, Kaushik S S, Ahn S, Veit-Haibach P, Delso G and Shanbhag D D 2016 Zero TE MR bone imaging in the head *Magn. Reson. Med.* **75** 107–14
Wollenweber S, Ambwani S, Delso G, Lonn A, Mullick R, Wiesinger F, Piti Z, Tari A, Novak G and Fidrich M 2013 Evaluation of an atlas-based PET head attenuation correction using PET/CT and MR patient data *IEEE Trans. Nucl. Sci.* **60** 3383–90
Wu Y, Ackerman J L, Chesler D A, Graham L, Wang Y and Glimcher M J 2003 Density of organic matrix of native mineralized bone measured by water-and fat-suppressed proton projection MRI *Magn. Reson. Med.* **50** 59–68
Zubal I G, Harrell C R, Smith E O, Rattner Z, Gindi G and Hoffer P B 1994 Computerized three-dimensional segmented human anatomy *Med. Phys.* **21** 299–302